Letter

Isotope shift of fine structure of Kr^+ and hyperfine structure of $^{83}Kr^+$ by strong-field ultrahigh-resolution Fourier-transform spectroscopy

Toshiaki Ando, Kana Yamada, Atsushi Iwasaki, and Kaoru Yamanouchi*,†

Department of Chemistry, School of Science, The University of Tokyo, 7-3-1 Hongo, Bunkyo-ku, Tokyo 113-0033, Japan

(Received 4 July 2024; accepted 18 March 2025; published 25 April 2025)

We determine the energies of hyperfine structure splitting of $^{83}Kr^+$ and isotope shifts in the fine structure splitting of Kr^+ with precision of sub-MHz ($\sim 10^{-5}$ cm^{-1}) by strong-field ultrahigh resolution Fourier-transform spectroscopy. From the splitting energies, we determine the hyperfine structure constants of $^{83}Kr^+$ and the isotope shift parameters of Kr^+. Based on the field shift parameters, we identify the deformation of the electron density distribution of the 4p orbital of Kr^+ originating from the relativistic effect.

DOI: 10.1103/PhysRevResearch.7.L022025

An isotope shift of atomic energy levels originates from the mass shift and the field shift [1]. The mass shift is caused by the difference in the mass of nuclei and the field shift originates from the difference in the size of the nuclei as well as from the difference in the electron density at the nuclei. To elucidate details of nuclear and electronic structures of atoms by the field shift, efforts have been made to record optical transitions of atomic species with high precision [2–6].

The field shift in the transition of atomic species between the spin-orbit sublevels of $^2P_{1/2}$ and $^2P_{3/2}$ is of particular interest because it originates from the deformation of $np_{1/2}$ orbital caused by the relativistic effect. The nonzero value of the field shift originating from the relativistic effect was identified for the first time in the 6p ^{2}P states of Ba^+ ($Z = 56$) in 1984 [7]. A few years later, an isotope shift ascribable to the nonzero value of the field shift parameter was identified for Fr ($Z = 87$) [8], but the field shift parameter was not determined because the transition was observed only for two isotopes of ^{212}Fr and ^{221}Fr. Since then, to the best of our knowledge, no report has been made on experimental determination of a nonzero value of the field shift for atomic species other than Ba^+ [9]. In 2020, the 4s $^2S_{1/2}-4p\,^2P_{1/2}$ and 4s $^2S_{1/2}-4p\,^2P_{3/2}$ transitions of Ca^+ ($Z = 20$) were measured with a precision of 0.1 MHz [10], but the relativistic effect resulting in the field shift was not identified because the natural linewidth ($\sim$23 MHz) of these transitions limits the precision of the measurements required to identify the effect of the field shift.

The field shift can also be examined by high-precision measurements of optical transitions involving the lowest fine structure sublevels, $^2P_{1/2}$ and $^2P_{3/2}$, of rare gas atom cations, such as Kr^+ ($Z = 36$) and Xe^+ ($Z = 54$). By pulsed-field-ionization zero-kinetic-energy (PFI-ZEKE) photoelectron spectroscopy of Kr [11–13], an extrapolation of the hyperfine structures of the high-lying Rydberg states of Kr to those of Kr^+ based on multichannel quantum defect theory (MQDT) and the isotope dependences of the ionization energies for $Kr^+(^2P_{3/2})$ [14] and $Kr^+(^2P_{1/2})$ [11] were determined with an uncertainty of $10^{-3}-10^{-4}$ cm^{-1}. However, the precision of the measurements was comparable with the magnitude of the isotope shifts ($\sim 10^{-3}$ cm^{-1}), and the field shift constant was not determined.

In 2021 [15], we determined the fine structure splitting energies of Ar^+, Kr^+ and Kr^{2+} with a relative precision of 10^{-7} by strong-field ultrahigh-resolution Fourier transform (SURF) spectroscopy [16]. In the SURF spectroscopy, which is an isotope selective and Doppler-free method and is a variant of quantum-beat spectroscopy, a pump laser pulse creates a coherent superposition of the $^2P_{1/2}$ and $^2P_{3/2}$ states of rare gas atom cations by strong-field ionization of rare gas atoms and a probe pulse further ionizes the rare gas atom cations to dications. The probability of the ionization by the probe pulse depends on the relative phase between the $^2P_{1/2}$ and $^2P_{3/2}$ state and the fine structure splitting energy was obtained by a Fourier transform of the ion yields of the resultant rare gas atom dications.

In the present study, we improve the spectral resolution and precision of SURF measurements of Kr by increasing the scanning range of the pump-probe delay by a factor of 26 using a long-arm interferometer. The hyperfine structure of $^{83}Kr^+$ is well resolved at the spectral resolution of 2.6×10^{-3} cm^{-1} so that the hyperfine structure constants of $^{83}Kr^+$ are determined. Furthermore, the isotope shifts are determined with the precision of $\sim 10^{-5}$ cm^{-1} so that isotope-shift parameters, i.e., a mass shift constant and a field shift constant, are determined from the fine structure splitting energies.

An output of a Ti:sapphire chirped-pulse amplification laser system (30 fs, $\sim$800 nm 0.45 mJ/pulse) is introduced into a hollow-core fiber filled with an Ar gas to broaden the spectral bandwidth covering the range of 550–1000 nm via self-phase modulation. The spectral phase is compensated by a set of chirped mirrors and the laser pulses are introduced

*Present address: Institute for Attosecond Laser Facility, The University of Tokyo, 7-3-1 Hongo, Bunkyo-ku, Tokyo 113-0033, Japan.
†Contact author: kaoru@chem.s.u-tokyo.ac.jp

Published by the American Physical Society under the terms of the Creative Commons Attribution 4.0 International license. Further distribution of this work must maintain attribution to the author(s) and the published article's title, journal citation, and DOI.

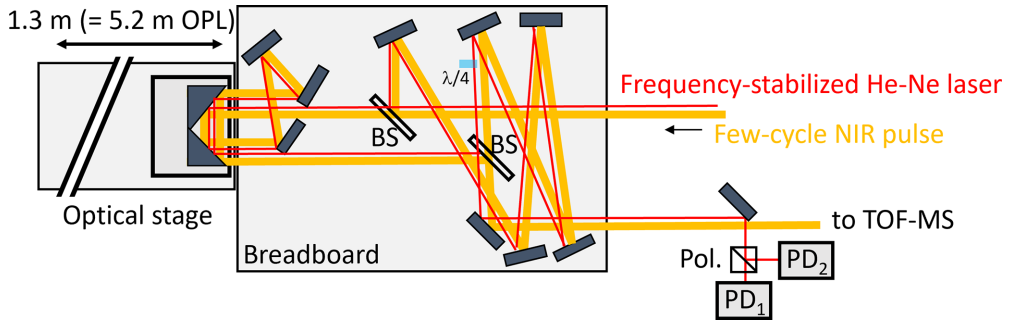


FIG. 1. Schematics of interferometer. BS: beam splitter, Orange lines: Optical path of few-cycle near-IR pulses, Red lines: Optical path of frequency-stabilized He-Ne laser pulses, QWP: quarter wave plate, Pol.: Polarizer, PD_1 and PD_2: Photodiodes.

into an interferometer placed in a vacuum chamber to create the pump and probe laser pulses as shown in Fig. 1. The pump-probe time delay, Δt, is controlled using a home-built optical stage driven by a stepping motor. A probe laser pulse is reflected twice by a high precision retroreflector (USHM, PLX Inc.) placed on the optical stage whose movable range is 1.3 m. Using this long-arm interferometer, the maximum optical-path difference of 5.2 m (= 1.3 m×4), corresponding to the maximum time delay of 17 ns, is achieved. In the present measurements, the maximum time delay is set to be 13 ns, corresponding to the resolution of a Fourier-transformed spectrum of 2.6×10^{-3} cm^{-1}. As shown in Fig. 1, to measure Δt, a frequency-stabilized He-Ne laser is introduced into the interferometer so that its axis becomes parallel to the pump and probe laser beam axes and only the He-Ne laser light passes through a quarter wave plate. The interferometric signals of the He-Ne laser light are detected by two photodiodes to measure the time delay (see Supplemental Material Sec. S1) [17]. The value of Δt obtained using the interferometric signal is a relative value and is set to be $\Delta t = 0$ ns at the timing when the pump and probe laser pulses interfere constructively so that the ion yields of Kr^{2+} becomes maximum.

The pulse duration of the compressed near-infrared (IR) laser pulses is measured to be 5.9 fs by a two-dimensional spectral shearing interferometer. The pump and probe laser pulses are introduced into a time-of-flight mass spectrometer and focused on an effusive beam of Kr. The focal radius of the laser pulses is 11(1) μm and the laser field intensity at the focus is estimated to be 8×10^{14} W/cm^2. In order to maximize the number of atoms interacting with both of the pump and probe laser pulses, the focal position of the probe pulse is set slightly (∼1 μm) downstream along the skimmed effusive beam of Kr with respect to the focal position of the pump pulse. The ion yields of the isotopes of $^{A}Kr^{2+}$ (A = 80, 82, 83, 84, and 86) are recorded shot-by-shot by a field-programmable gate array (FPGA)-based transient digitizer and the interferometric signal of the He-Ne laser light are recorded by a FPGA-based A/D converter. Because Δt is recorded with a sampling rate of 40 kHz, which is much faster than the resonant frequencies of optical elements, mechanical vibrations of the optical elements in the interferometer do not affect the precision of Δt.

Figure 2(a) shows the Fourier transform of the ion yields of $^{84}Kr^{2+}$. As explained in the previous study [15], the three peaks in the spectrum, assigned to the quantum beats of $^{84}Kr^{+}(^{2}P_{1/2}–^{2}P_{3/2})$, $^{84}Kr^{2+}(^{3}P_{1}–^{3}P_{2})$, and $^{84}Kr^{2+}(^{3}P_{0}–^{3}P_{2})$, show that the pump laser pulse creates an electronic wave packet of Kr^{+} and that of Kr^{2+} by the ion-

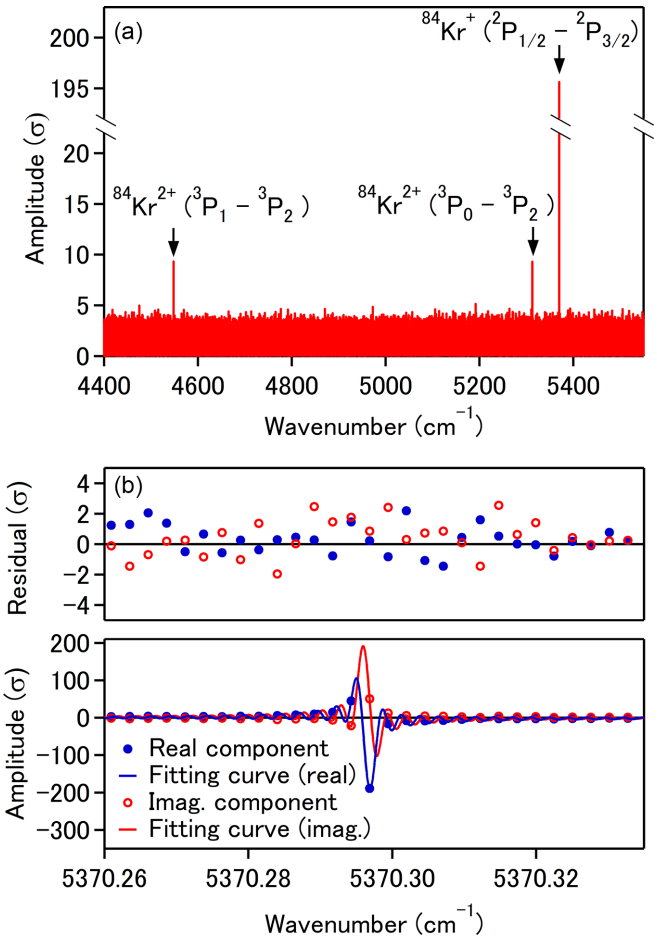


FIG. 2. (a) Fourier transform of the ion yields of $^{84}Kr^{2+}$ in the time delay range of 0.15 ns < Δt < 13.15 ns. The amplitude of the spectrum is normalized by the white noise level (σ), which is defined as the root mean square of the spectrum in the range between 4600 and 5200 cm^{-1}. (b) Lower panel: Best-fit curves for the real and imaginary components obtained by a least-squares fit to the peak of the quantum beat between the $^{2}P_{1/2}$ and $^{2}P_{3/2}$ states of $^{84}Kr^{+}$. Upper panel: Residuals of the least-squares fit.

ization of Kr and that the probe pulse projects the motion of the electron wave packet onto the ion yields of Kr^{2+} by the sequential ionization of Kr^+ and Kr^{2+}. As shown in Fig. 2(b), the $^2P_{1/2} - {}^2P_{3/2}$ peak of $^{84}Kr^+$ is fitted by

$$f_{84}(\omega) = Ie^{-i\theta} G_\omega((\omega - \omega_0), \delta x, \Delta x), \tag{1}$$

where I, ω_0, θ, δx, and Δx are the fitting parameters of the peak amplitude, the angular frequency of the peak, the phase of the peak, the difference of the focal position of the pump and probe pulses on the x axis, and the focal radius of the laser pulses, respectively. $G_\omega(\omega, \delta x, \Delta x)$ is the Fourier transform of a slowly varying envelope function, $G_t(t, \delta x, \Delta x)$, which is normalized at $\omega = 0$ so that $G_\omega(0, \delta x, \Delta x) = 1$. The variation of the envelope function is ascribed to the variation of the number of Kr^+ ions in the focal region originating from the translational motion of the sample gas along the x axis (see Supplemental Material Sec. S2 [17]).

The SURF spectrum is scaled for the calibration so that ω_0 becomes 5370.29642 cm^{-1}, which is obtained in our previous study using the reference frequencies of H_2 [15]. Because the uncertainty associated with ω_0 is 5×10^{-4} cm^{-1} [15], the relative systematic uncertainty in the calibration of the angular frequencies of the present SURF measurement is 5×10^{-4} $cm^{-1}/5370$ $cm^{-1} = 93\times10^{-9}$, which is negligibly small compared with the relative statistical uncertainties of the hyperfine splitting energies and the isotope splitting energies as discussed below.

The peaks corresponding to the quantum beat of Kr^{2+} shown in Fig. 2(a) are also fitted using Eq. (1), and the energy spacing between the $^3P_1$ and $^3P_2$ levels of Kr^{2+} is determined to be 4548.21818 cm^{-1} with the statistical and systematic uncertainties of $\sigma_{sta} = 15\times10^{-5}$ cm^{-1} and $\sigma_{sys} = 42\times10^{-5}$ cm^{-1} and that between the $^3P_0$ and $^3P_2$ levels of Kr^{2+} is determined to be 5312.80447 cm^{-1} with the statistical and systematic uncertainties of $\sigma_{sta} = 15\times10^{-5}$ cm^{-1} and $\sigma_{sys} = 49\times10^{-5}$ cm^{-1}. These energy spacings are in good agreement with those obtained by our previous study [15] and the precision in the present measurements is better than that in our previous measurements by a factor of eight.

Figure 3(a) shows the Fourier transform of the ion yields of $^{83}Kr^{2+}$ at around 5370 cm^{-1}. The eight peaks appearing in the spectrum are assigned to the quantum beats between the hyperfine structure (HFS) sublevels of $J = 3/2$ states and $J = 1/2$ states of Kr^+. By assuming that the ionization probability varies depending on the electron configuration, the amplitudes of a Fourier-transformed peak can be given by [15]

$$A(F, F') \propto \sqrt{(2F+1)(2F'+1)} \sum_{m_I,\, m_F, m_{F'}} \left\{ \begin{pmatrix} \frac{3}{2} J & I & F \\ \frac{1}{2} m_J & m_I & -m_F \end{pmatrix} \begin{pmatrix} \frac{1}{2} J & I & F' \\ \frac{1}{2} m_J & m_I & -m_{F'} \end{pmatrix} - \begin{pmatrix} \frac{3}{2} J & I & F \\ -\frac{1}{2} m_J & m_I + 1 & -m_F \end{pmatrix} \begin{pmatrix} \frac{1}{2} J & I & F' \\ -\frac{1}{2} m_J & m_I + 1 & -m_{F'} \end{pmatrix} \right\}^2. \tag{2}$$

The resultant line strengths agree well with the experimental results as shown in Fig. 3(a). The energies of the hyperfine levels can be expressed as

$$E(J, F) = E_{SO}(J(J+1) - L(L+1) - S(S+1)) + A_J \frac{C}{2} + B_J \frac{\frac{3}{4}C(C+1) - I(I+1)J(J+1)}{2I(2I-1)J(2J-1)}, \tag{3}$$

where $C = F(F+1) - I(I+1) - J(J+1)$, and E_{SO}, A_J, and B_J are the spin-orbit coupling constant, the magnetic dipole coupling constant, and the electric quadrupole coupling constant, respectively, which are hereafter referred to as HFS constants. We neglect here the coupling of $J = 1/2$ state and $J = 3/2$ state by the hyperfine interaction because the level energies are influenced only at most of the order of 10^{-7} cm^{-1}, which is negligibly small compared with the statistical uncertainties in the present measurements. To obtain the hyperfine energy spacings, $\Delta E_{F,F'} = E(J = 1/2, F') - E(J = 3/2, F)$, the spectrum of $^{83}Kr^+$ composed of these eight peaks is fitted by

$$f_{83}(\omega) = \sum_{F,F'} I_{F,F'} e^{-i\theta_\omega(F,F')} G_\omega((\omega - \omega_{F,F'}), \delta x, \Delta x), \tag{4}$$

where F and F' are the total angular momentum quantum numbers of the lower ($J = 3/2$) and upper ($J = 1/2$) states, respectively. $I_{F,F'}$, $\theta_\omega(F, F')$ and $\omega_{F,F'}$ are the peak amplitudes, the phase of the peaks, and the energy intervals represented by the angular frequencies. After the least-squares fit, we obtain the phase at $t = 0$, $\theta_t(F, F')$ from the phase of the peaks in the frequency domain, $\theta_\omega(F, F')$, using the relationship,

$$\theta_t(F, F') + \omega_{F,F'} t_{min} = \theta_\omega(F, F'), \tag{5}$$

where $t_{min} = \sim150$ ps is the minimum value of the Fourier transform range. The systematic uncertainty of t_{min} is ~1 fs, which corresponds to the uncertainty of $t = 0$ determined as the timing when the ion yields of Kr^{2+} takes the maximum value. The parameters obtained by the least-squares fits are summarized in Table I. The best-fit peak amplitudes, $I_{F,F'}$, agree well with the amplitudes, $A(F, F')$, calculated using Eq. (2). In Table I, the relative phases measured from the phase for $(F, F') = (6, 4)$, $\theta_t(F, F') - \theta_t(6, 4)$, are plotted to remove the systematic uncertainty originating from the uncertainty of t_{min}. As shown in Table S1, the phase values are close to 0, showing that the all the quantum beats constructively interfere at $t \sim 0$, which supports our model in which the $^2P(m_L = 0)$ state is prepared by the pump pulse as a coherent superposition of the HFS sublevels.

The HFS constants are obtained by least-squares fits using Eq. (3). As shown in Table II, the present value of $A_{1/2}$ is in good agreement with the literature value [11] and the

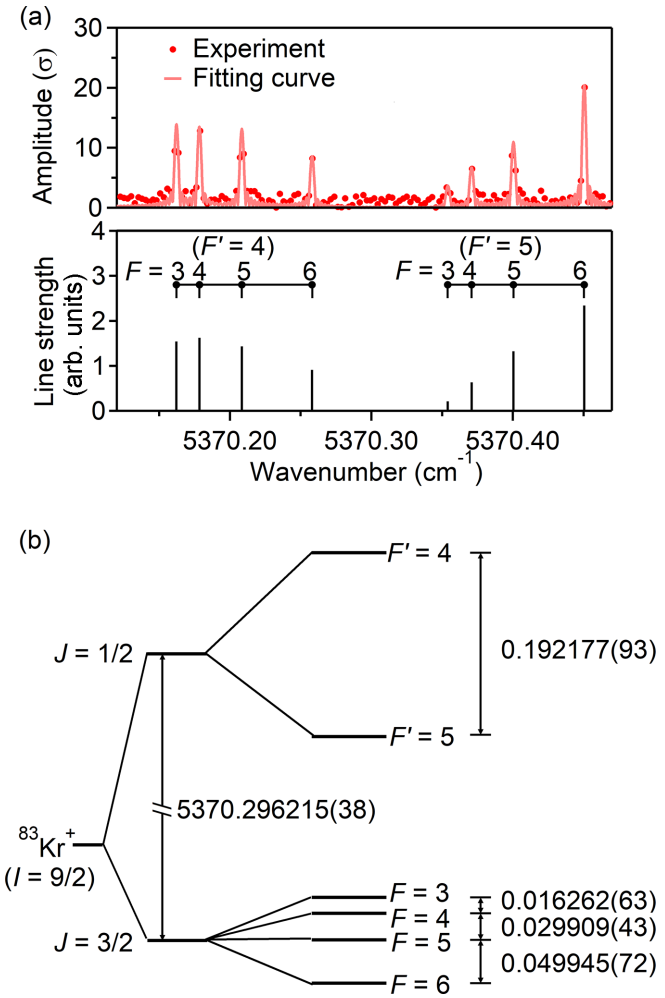


FIG. 3. (a) Upper panel: Fourier transform of the ion yields of $^{83}Kr^{2+}$ (red dots) and the result of the least-squares fit to the experimental data (red curve). Lower panel: The line strengths calculated using Eq. (2). (b) Energy level separations in the HFS of $^{83}Kr^{+}$ obtained from the SURF spectrum.

precision is improved by 25 times. As for $A_{3/2}$ and $B_{3/2}$, the present values are also in good agreement with those reported in Ref. [12]. The precisions of $A_{3/2}$ and $B_{3/2}$ are improved by four times and eight times, respectively. On the other hand, the present values of $A_{3/2}$ and $B_{3/2}$ exhibit certain deviations from those reported in Ref. [13]. The relative uncertainty, 0.53%, of $B_{3/2} = eQq$ obtained in the present study is close to the relative uncertainty, 0.39%, of the nuclear quadrupole moment Q (=258(1) mb), calculated using the eQq value for the Kr nucleus in KrD^+ molecule obtained spectroscopically [18] and the theoretically calculated electric field gradient q at the Kr nucleus of KrD^+ [19].

The time-dependent ion yield of $^{83}Kr^{2+}$ can be retrieved as shown in Fig. 4(a) using the formula, $Y(t) = \sum_{F,\,F'} I_{F,F'}\cos(\omega_{F,F'}t + \theta_t(F,F'))$, with the results of the least-squares fit listed in Table I. It is found that the ion yield oscillates with a period of ~6.2 fs and that the oscillation amplitude is modulated in a complex manner in the wide range of time up to more than 12 ns as shown in Fig. 4(a). On the other hand, the oscillation of the population in the $^2P(m_L = \pm 1)$ state of $^{83}Kr^+$ are calculated using the formula, $P(t) = \sum_{F,\,F'} A(F,F')\cos(\omega_{F,F'}t + \pi)$, as shown in Fig. 4(b). The fact that Fig. 4(b) reproduces with high fidelity the temporal variation of the yield of $^{83}Kr^{2+}$ shown in Fig. 4(a) confirms that the temporal variation of the population in the $^2P(m_L = \pm 1)$ state of $^{83}Kr^+$ is retrieved by the SURF measurements of the yield of $^{83}Kr^{2+}$.

The fine structure splitting energy of the isotopes (A = 80, 82, 84, and 86) are determined as shown in Table III by the least-squares fits to the peak in the Fourier transform of the ion yields of Kr^{2+}. In the case of $^{83}Kr^+$, a weighted average of the HFS frequencies is adopted. The statistical uncertainty is only in the range of 10^{-5}–10^{-6} cm^{-1} thanks to the high signal-to-noise ratio as can be seen in Fig. 2(b) for $^{84}Kr^+$. The systematic uncertainty (5×10^{-4} cm^{-1}) is much larger than the statistical uncertainty, but the systematic uncertainty does not influence the isotope shift, δE^{A86}. The isotope shift, $\delta E^{AA'} = E_A - E_{A'}$, defined as a shift of the energy E_A of an isotope A from the energy E'_A of another isotope A' is expressed as

$$\delta E^{AA'} = \frac{K}{\mu^{AA'}} + F_S \delta\langle r_c^2\rangle^{AA'}, \tag{6}$$

where the first term in the left-hand side represents a mass shift and the second term represents the field shift. In the first term, $(\mu^{AA'})^{-1}$ is given by $(\mu^{AA'})^{-1} = (m_{A'})^{-1} - (m_A)^{-1}$ using the masses, m_A and $m_{A'}$, of nuclei A and A' [21] and K is

TABLE I. Results of the least-squares fit to the hyperfine structure of $^{83}Kr^+$.

F-F'	$\omega_{F,F'}$/cm^{-1}	$\theta_t(F,F') - \theta_t(6,4)$ /rad	$I_{F,F'}$[a]	$A(F,F')$[a,b]
3–5	5 370.162 205(83)	0.18(14)	15. 5(9)	15.4
4–5	5 370.178 332(84)	0.14(15)	15.2(9)	16.2
5–5	5 370.208 372(92)	−0.09(15)	14.5(9)	14.3
6–5	5 370.258 12(14)	0.35(22)	9.0(9)	9.1
3–4	5 370.354 03(36)	0.26(51)	3.6(9)	2.1
4–4	5 370.370 67(18)	−0.08(27)	7.1(9)	6.3
5–4	5 370.400 39(10)	0.17(16)	12.8(9)	13.2
6–4	5 370.450 465(58)	0	22.4(9)	23.4

[a]Normalized so that the sum is 100.
[b]Calculated by Eq. (2).

TABLE II. Comparison of the HFS constants ($/cm^{-1}$) of $^{83}Kr^+$.

		MQDT analysis of PFI-ZEKE spectra			
	Present study	Ref. [12]	Ref. [13]	Ref. [11]	GRASP2018 [20]
$A_{1/2}$	−0.038435(19)			−0.0385(5)	−0.035
$A_{3/2}$	−0.006621(8)	−0.00661(3)	−0.00616(4)		−0.0063
$B_{3/2}$	−0.015331(82)	−0.0154(7)	−0.0127(4)		−0.013

the mass shift constant. In the second term, F_S is the field shift constant, which is proportional to the difference in the electron density at the nuclei, $\rho_{J=1/2}(0) - \rho_{J=3/2}(0)$ and $\delta\langle r_c^2\rangle^{AA'}$ is the difference in the effective charge radius of the nuclei [22] defined as $\delta\langle r_c^2\rangle^{AA'} = \langle r_c^2\rangle^{A} - \langle r_c^2\rangle^{A'}$. As shown in Table III, the isotope shifts of the fine structure splitting energies are determined in the present study with much higher precision than those determined in the previous studies [11,14]. The mass-weighted isotope shifts are plotted in Fig. 5 as a function of the mass-weighted value of $\delta\langle r_c^2\rangle^{AA'}$. By a least-squares fit to Eq. (6), the isotope shift parameters are determined to be $K = 1.70(17)$ cm^{-1} u (= 51.0(51) GHz u) and $F_S = -1.9(13)\times10^{-3}$ cm^{-1}/fm^2 (= –57(39) MHz/fm^2).

There are two origins for a nonzero value of F_S, that is, an electron correlation and a relativistic effect. In the case of transition metals, e.g., the electron correlation is a dominant origin because of the strong electron correlation in the d orbitals [23,24]. In the present case of Kr^+, because the electron configurations of the $^2P_{1/2}$ and $^2P_{3/2}$ states are well represented by $(4p_{1/2})^1(4p_{3/2})^4$ and $(4p_{1/2})^2(4p_{3/2})^3$, respectively, the contribution of the electron correlation is small. In the nonrelativistic limit, the electron densities of $4p_{1/2}$ and $4p_{3/2}$ orbitals at the origin are 0, and consequently, the field shift parameter is 0. However, when the relativistic effect is taken into account, the electron density of the $p_{1/2}$ orbital at the nuclei, $\rho_{j=1/2}(0)$, is larger than that of the $p_{3/2}$ orbital, $\rho_{j=3/2}(0)$, that is, $\rho_{j=1/2}(0) > \rho_{j=3/2}(0)$. This is because an s-orbital character is mixed in the electron density distribution of the $p_{1/2}$ orbital whereas a d-orbital character is mixed in the $p_{3/2}$ orbital.

The fact that the experimentally determined field shift constant, $F_S = -1.9(13)\times10^{-3}$ cm^{-1}/fm^2, is negative shows that the electron density at the nuclei of the $P_{3/2}$ state $(4p_{1/2})^2(4p_{3/2})^3$ is larger than that of the $P_{1/2}$ state $(4p_{1/2})^1(4p_{3/2})^4$. This is consistent with $\rho_{j=1/2}(0) > \rho_{j=3/2}(0)$, originating from the relativistic effect. The HFS constants and the isotope shift parameters are numerically calculated by a multi-configuration Dirac-Hartree-Fock (MCDHF) method using GRASP2018 (General Relativistic Atomic Structure Package 2018) [20]. After the MCDHF computations for the atomic state functions of the $^2P_{1/2}$ and $^2P_{3/2}$ states, the mass shift parameter and the difference in the electron density are calculated using the Relativistic Isotope Shifts 4 (RIS4) program [25]. The field shift parameter is obtained using a formula, $F = \pi(\rho_{J=1/2}(0) - \rho_{J=3/2}(0))f(Z)/Z$, where $f(Z) = 2.1$ GHz/fm^2 is adopted by assuming that the nuclear is a uniformly charged sphere [26,27]. The calculated HFS constants agree with the experimental values with the deviations of 10–20%, and the isotope shift parameters are calculated to be $K = 1.3$ cm^{-1} u (= 39 GHz u) and $F = -1.6\times10^{-3}$ cm^{-1}/fm^2 (= −47 MHz/fm^2), which are consistent with the experimentally obtained values.

In summary, we have performed SURF spectroscopy of Kr^+ with sub-100 MHz resolution and sub-MHz precision and observed the isotope shifts in the fine structure splitting energies for Kr^+ and the HFS of $^{83}Kr^+$. The precision of hyperfine coupling constants of $^{83}Kr^+$ has been improved by a factor of 4–25 and the negative value of the field shift constant obtained from the fine structure splitting energies reflects the

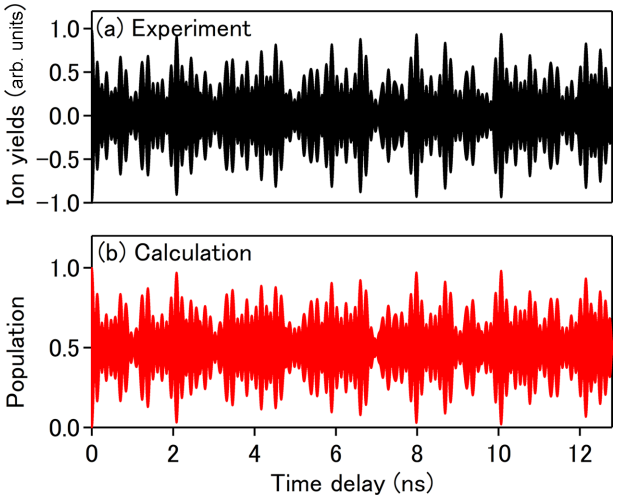


FIG. 4. (a) Oscillation of the ion yields of $^{83}Kr^{2+}$ extracted from the SURF spectrum. (b) Oscillation of the synthesized population of the $^2P(m_L = \pm1)$ state of $^{83}Kr^+$.

TABLE III. The fine structure splitting energy of the isotopes.

	Present study		Previous studies[b]
A	Wave number/cm^{-1}	$\delta E^{A\,86}/10^{-4}$ cm^{-1}	$\delta E^{A\,86}/10^{-4}$ cm^{-1}
78			−1.4(97)
80	5 370.295 261(33)	−17.07(34)	−5.2(87)
82	5 370.295 850(14)	−11.18(17)	−12.8(85)
83	5 370.296 215(38)[a]	−7.53(39)	–
84	5 370.296 420(6)	−5.48(12)	−2.1(60)
86	5 370.296 968(10)	0	0

[a]Nuclear-spin averaged frequency.
[b]Obtained from the ionization energy of Kr to $Kr^+(^2P_{3/2})$ [14] and that to $Kr^+(^2P_{1/2})$ [11].

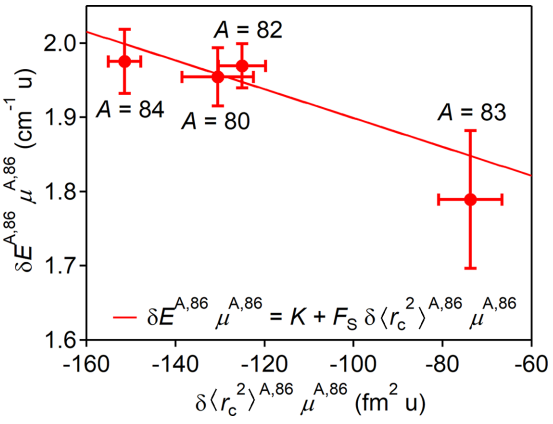


FIG. 5. Mass-weighted isotope shift of the $^2P_{1/2} - {}^2P_{3/2}$ energy spacing of Kr^+ plotted as a function of mass-weighted $\delta\langle r_c^2\rangle^{A,A'}$.

distortion of the electron density of the 4p-orbital by the relativistic effect. The precision of the present measurement, limited by the length of the arm of the interferometer, can be raised by at least two orders of magnitude by introducing a frequency-comb technique [28]. The SURF spectroscopy, by which the fine structure splitting energies for Kr^{2+} as well as for Kr^+ can be determined with high precision, will be one of the promising approaches to the discussion of the bosonic interaction beyond the standard model based on a nonlinearity in a King plot [29–35].

We are grateful to Dr. J. Nishikawa in National Astronomical Observatory of Japan for his valuable guidance on the construction of the long-arm interferometer. The present research was supported by JSPS KAKENHI Grants No. 15H05696, No. 19K15500, No. 24K08335, and No. 20H00371.

[1] W. H. King, *Isotope Shifts in Atomic Spectra* (Springer, Boston, MA, 1984).

[2] J. Z. Han *et al.*, Isotope shift factors for the Cd^+ $5s\,^2S_{1/2} \rightarrow 5p\,^2P_{3/2}$ transition and determination of Cd nuclear charge radii, Phys. Rev. Res. **4**, 033049 (2022).

[3] G. Penyazkov, S. D. Prosnyak, A. E. Barzakh, and L. V. Skripnikov, Refined theoretical values of field and mass isotope shifts in thallium to extract charge radii of Tl isotopes, J. Chem. Phys. **158**, 114110 (2023).

[4] P. Hao *et al.*, Precision measurement of $^{25}Mg^+$-ion D_1 and D_2 transition frequencies, Phys. Rev. A **107**, L020803 (2023).

[5] K. König *et al.*, Nuclear charge radii of silicon isotopes, Phys. Rev. Lett. **132**, 162502 (2024).

[6] B. Rahaman, S. C. Wright, and S. Dutta, Observation of quantum interference of optical transition pathways in Doppler-free two-photon spectroscopy and implications for precision measurements, Phys. Rev. A **109**, 042820 (2024).

[7] K. Wendt, S. A. Ahmad, F. Buchinger, A. C. Mueller, R. Neugart, and E.-W. Otten, Relativistic J-dependence of the isotope shift in the 6s-6p doublet of Ba II, Z. Phys. A **318**, 125 (1984).

[8] J. Bauche *et al.*, Accurate wavenumbers of the first resonance doublet of francium atoms and relativistic contribution to isotope shifts in the resonance doublets of francium and caesium atoms, J. Phys. B **19**, L593 (1986).

[9] P. Imgram, K. König, J. Krämer, T. Ratajczyk, R. A. Müller, A. Surzhykov, and W. Nörtershäuser, Collinear laser spectroscopy at ion-trap accuracy: Transition frequencies and isotope shifts in the $6s\,^2S_{1/2} \rightarrow 6p\,^2P_{1/2,3/2}$ transitions in Ba^+, Phys. Rev. A **99**, 012511 (2019).

[10] P. Müller, K. König, P. Imgram, J. Krämer, and W. Nörtershäuser, Collinear laser spectroscopy of Ca^+: Solving the field-shift puzzle of the $4s\,^2S_{1/2} \rightarrow 4p\,^2P_{1/2,3/2}$ transitions, Phys. Rev. Res. **2**, 043351 (2020).

[11] Th. A. Paul, J. Liu, and F. Merkt, Nuclear-spin effects in the photoionization of krypton, Phys. Rev. A **79**, 022505 (2009).

[12] M. Schäfer and F. Merkt, Millimeter-wave spectroscopy and multichannel quantum-defect-theory analysis of high Rydberg states of krypton: The hyperfine structure of $^{83}Kr^+$, Phys. Rev. A **74**, 062506 (2006).

[13] H. J. Wörner, U. Hollenstein, and F. Merkt, Multichannel quantum defect theory and high-resolution spectroscopy of the hyperfine structure of high Rydberg states of $^{83}Kr^+$, Phys. Rev. A **68**, 032510 (2003).

[14] U. Hollenstein, R. Seiler, and F. Merkt, Determination of the ionization energy of krypton by Rydberg-state-resolved threshold-ionization spectroscopy, J. Phys. B **36**, 893 (2003).

[15] T. Ando, A. Liu, N. Negishi, A. Iwasaki, and K. Yamanouchi, Spin-orbit splitting of Ar^+, Kr^+, and Kr^{2+} determined by strong-field ultrahigh-resolution Fourier-transform spectroscopy, Phys. Rev. A **104**, 033516 (2021).

[16] T. Ando, A. Iwasaki, and K. Yamanouchi, Strong-field fourier transform vibrational spectroscopy of D_2^+ using few-cycle near-infrared laser pulse, Phys. Rev. Lett. **120**, 263002 (2018).

[17] See Supplemental Material at http://link.aps.org/supplemental/10.1103/PhysRevResearch.7.L022025 for the measurement of the time delay, the fitting procedure, and the analysis of the isotope shift.

[18] H. E. Warner, W. T. Conner, and R. C. Woods, The lowest rotational transition of several isotopic forms of KrD^+, J. Chem. Phys. **81**, 5413 (1984).

[19] V. Kellö, P. Pyykkö, and A. J. Sadlej, Nuclear quadrupole moments of Kr and Xe from molecular data, Chem. Phys. Lett. **346**, 155 (2001).

[20] C. Froese Fischer, G. Gaigalas, P. Jönsson, and J. Bieroń, GRASP2018—A fortran 95 version of the general relativistic atomic structure package, Comput. Phys. Commun. **237**, 184 (2019).

[21] J. Emsley, *The Elements* (Oxford University Press, New York, 1998).

[22] I. Angeli and K. P. Marinova, Table of experimental nuclear ground state charge radii: An update, At. Data Nucl. Data Tables **99**, 69 (2013).

[23] Y. P. Gangrsky, K. P. Marinova, and S. G. Zemlyanoi, J dependences of the isotope shifts in Ti I $3d^2\,4s^2\,a^3P$ and $3d^3\,4p\,y^3D^O$ terms, J. Phys. B **28**, 957 (1995).

[24] A. O. Neely, K. Cassella, S. Eustice, and D. M. Stamper-Kurn, Isotope shifts in the metastable a^5F and excited y^5G^O terms of atomic titanium, Phys. Rev. A **103**, 032818 (2021).

[25] J. Ekman, P. Jönsson, M. Godefroid, C. Nazé, G. Gaigalas, and J. Bieroń, RIS 4: A program for relativistic isotope shift calculations, Comput. Phys. Commun. **235**, 433 (2019).

[26] S. A. Blundell, P. E. G. Baird, C. W. P. Palmer, D. N. Stacey, G. K. Woodgate, and D. Zimmermann, A re-evaluation of isotope shift constants, Z. Phys. A **321**, 31 (1985).

[27] M. Keim, E. Arnold, W. Borchers, U. Georg, A. Klein, R. Neugart, L. Vermeeren, R. E. Silverans, and P. Lievens, Laser-spectroscopy measurements of 72–96 Kr spins, moments and charge radii, Nucl. Phys. A **586**, 219 (1995).

[28] C. Schröter, J. C. Lee, and T. Schultz, Mass-correlated rotational Raman spectra with high resolution, broad bandwidth, and absolute frequency accuracy, Proc. Natl. Acad. Sci. USA **115**, 5072 (2018).

[29] C. Solaro, S. Meyer, K. Fisher, J. C. Berengut, E. Fuchs, and M. Drewsen, Improved isotope-shift-based bounds on bosons beyond the standard model through measurements of the $^2D_{3/2} - ^2D_{5/2}$ interval in Ca^+, Phys. Rev. Lett. **125**, 123003 (2020).

[30] V. Debierre, N. S. Oreshkina, I. A. Valuev, Z. Harman, and C. H. Keitel, Testing standard-model extensions with isotope shifts in few-electron ions, Phys. Rev. A **106**, 062801 (2022).

[31] J. Hur *et al.*, Evidence of two-source king plot nonlinearity in spectroscopic search for new boson, Phys. Rev. Lett. **128**, 163201 (2022).

[32] N. L. Figueroa, J. C. Berengut, V. A. Dzuba, V. V. Flambaum, D. Budker, and D. Antypas, Precision determination of isotope shifts in ytterbium and implications for new physics, Phys. Rev. Lett. **128**, 073001 (2022).

[33] K. Ono, Y. Saito, T. Ishiyama, T. Higomoto, T. Takano, Y. Takasu, Y. Yamamoto, M. Tanaka, and Y. Takahashi, Observation of nonlinearity of generalized king plot in the search for new boson, Phys. Rev. X **12**, 021033 (2022).

[34] N.-H. Rehbehn, M. K. Rosner, J. C. Berengut, P. O. Schmidt, T. Pfeifer, M. F. Gu, and J. R. Crespo López-urrutia, narrow and ultranarrow transitions in highly charged Xe ions as probes of fifth forces, Phys. Rev. Lett. **131**, 161803 (2023).

[35] S. Gravina, N. A. Chishti, S. Di Bernardo, E. Fasci, A. Castrillo, A. Laliotis, and L. Gianfrani, Comb-referenced doppler-free spectrometry of the ^{200}Hg and ^{202}Hg intercombination line at 254 nm, Phys. Rev. Lett. **132**, 213001 (2024).